

Time series learning in a many-body Rydberg system with emergent collective nonlinearity

Zongkai Liu^{1,2,*;§}, Qiming Ren^{1,2;§}, Chris Nill^{3,4,†;§}, Albert Cabot³, Wei Xia⁵, Yanjie Tong^{1,2}, Huizhen Wang^{1,2}, Wenguang Yang^{1,2}, Junyao Xie^{1,2}, Mingyong Jing^{1,2}, Hao Zhang^{1,2}, Liantuan Xiao^{1,2}, Suotang Jia^{1,2}, Igor Lesanovsky^{3,6}, and Linjie Zhang^{1,2,‡}

¹State Key Laboratory of Quantum Optics Technologies and Devices, Taiyuan Shanxi, 030006, China.

²Collaborative Innovation Center of Extreme Optics, Shanxi University, Taiyuan, Shanxi 030006, China.

³Institut für Theoretische Physik and Center for Integrated Quantum Science and Technology (IQST), Eberhard Karls Universität Tübingen, Auf der Morgenstelle, 14, 72076, Tübingen, Germany

⁴Institute for Applied Physics, University of Bonn, Wegelerstraße 8, 53115 Bonn, Germany

⁵Department of Physics and The Hong Kong Institute of Quantum Information Science and Technology, The Chinese University of Hong Kong, Shatin, New Territories, Hong Kong, 999077, China and

⁶School of Physics and Astronomy and Centre for the Mathematics and Theoretical Physics of Quantum Non-Equilibrium Systems, The University of Nottingham, Nottingham, NG7 2RD, United Kingdom

(Dated: November 20, 2025)

Interacting Rydberg atoms constitute a versatile platform for the realization of non-equilibrium states of matter. Close to phase transitions, they respond collectively to external perturbations, which can be harnessed for technological applications in the domain of quantum metrology and sensing. Owing to the controllable complexity and straightforward interpretability of Rydberg atoms, we can observe and tune the emergent collective nonlinearity. Here, we investigate the application of an interacting Rydberg vapour for the purpose of time series prediction. The vapour is driven by a laser field whose Rabi frequency is modulated in order to input the time series. We find that close to a non-equilibrium phase transition, where collective effects are amplified, the capability of the system to learn the input becomes enhanced. This is reflected in an increase of the accuracy with which future values of the time series can be predicted. Using the Lorenz time series and temperature data as examples, our work demonstrates how emergent phenomena enhance the capability of noisy many-body quantum systems for data processing and forecasting.

I. INTRODUCTION

Computation, information processing, and dynamics in many-body systems are inherently intertwined. One paradigmatic example is the Hopfield network [1], whose architecture, energy function, and memory retrieval are directly derived from the Ising model. Other examples include swarm intelligence algorithms, such as particle swarm optimization [2–4] and ant colony optimization [5, 6]. These systems exploit collective interactions across scales to exhibit emergent computational capabilities, where nonlinear coupling between microscopic degrees of freedom generates information-processing capabilities. This interplay underscores both the potential of physical systems as computational platforms and the need to decode how collective behaviour enables specific computational tasks.

A particularly relevant and challenging task is time-series prediction of complex systems, for example chaotic dynamics such as the Lorenz attractor [7, 8] or weather

forecasting [9]. A computational framework that has proven effective for such problems is reservoir computing [10–13]. In reservoir computing, only a linear read-out layer is trained, while the high-dimensional, nonlinear reservoir dynamics remain fixed. This significantly simplifies training, as it avoids tuning a large number of internal degrees of freedom and instead leverages the computational power of the intrinsic dynamics of the system, provided they are sufficiently rich [14–16]. Reservoir computing has been implemented in a variety of settings, such as in echo state networks [17–19] and liquid state machines [20] as well as in physical systems such as delay-based electronic circuit reservoirs [21], and quantum reservoir computing platforms [22–24]. Despite this diversity, understanding the fundamental mechanisms that endow complex physical reservoirs with learning and prediction capabilities remains subject to current research [25].

Thermal Rydberg vapours are a promising platform in this context. These many-body platforms are known to exhibit a rich phase diagram with complex internal dynamics, as extensively studied theoretically [26–30] and demonstrated experimentally [31–35]. These features make Rydberg ensembles attractive candidates as platforms for reservoir computing, and, at the same time, ideal systems for probing the microscopic origin of learn-

* lzk1997@sxu.edu.cn

† chris.nill@uni-tuebingen.de

‡ zlj@sxu.edu.cn

§ Z.L., Q.R., and C.N. contribute equally to this work.

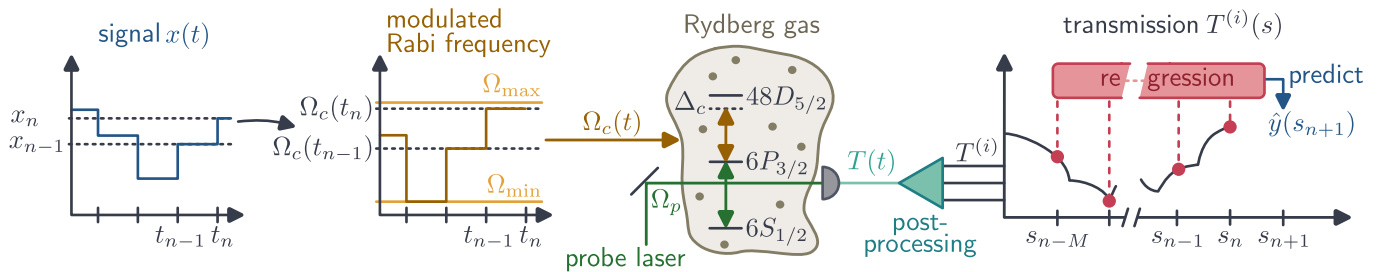


Figure 1. **Time series prediction with a Rydberg vapour.** The time-dependent input signal $x(t)$ is sampled at discrete time steps t_n , yielding a step-wise constant function with values $x_n = x(t_n)$. The signal is converted into the Rabi frequency $\Omega_c(t_n)$ of the coupling laser, which couples the intermediate state $6P_{3/2}$ to the Rydberg state $48D_{5/2}$ detuned by Δ_c . This Rabi frequency ranges within the interval $[\Omega_{\min}, \Omega_{\max}]$. The caesium (Cs) atoms are first excited by a probe laser with a constant Rabi frequency Ω_p , which drives the transition from the ground state $6S_{1/2}$ to the intermediate $6P_{3/2}$. Subsequently, the atoms are excited by the modulated coupling laser. The optical response of the Cs vapour is measured by monitoring the transmission $T(t)$ of this probe laser. The measured transmission $T(t)$ is post-processed using a Savitzky-Golay filter and down-sampled by a factor of 20, yielding the transmission signals $T^{(i)} = T(t_{i+20n})$. Here, $i \in [1, 20]$ labels the index of the downsampled time series and $s_n = t_{i+20n}$ denotes the corresponding time. The transmission signal within the time interval $[s_{n-M}, s_n]$ is used to predict the signal $x(s_{n+1})$ (denoted as $\hat{y}(s_{n+1})$). This prediction is generated by a linear regression layer, which was previously trained (see text for details).

ing capabilities in complex many-body dynamics at the atomic level.

In this work, we exploit the response of a Rydberg vapour as a physical reservoir for time-series prediction. The experimental control over the collective behaviour of the system enables us to systematically analyse how its internal dynamics give rise to learning capabilities. We find that the learning performance is improved in the vicinity of a phase transition, where nonlinear and collective responses are strongly amplified in the Rydberg vapour. This behaviour is in good agreement with a corresponding theoretical minimal model, providing insight into how critical many-body dynamics augment the computational power of physical reservoirs.

II. EXPERIMENT

Before discussing the detailed experimental results, we briefly outline the overall aim and approach of our study. The experiment is designed to test whether the vapour of interacting Rydberg atoms can process and predict time-dependent input signals by exploiting its intrinsic nonlinear and collective dynamics, see Fig. 1. To achieve this, we encode time-series data $x(t)$ in an amplitude modulation of the coupling laser's Rabi frequency Ω_c . The coupling laser drives the atomic ensemble under fixed detuning Δ_c and serves as input signal. The transmission of a probe laser serves as the measurable output that reflects how the Rydberg vapour responds and processes the input information. We record this transmission signal as a time series and use it as input to a simple linear regression model that is trained to predict future values of the original time series $x(t)$. By comparing the system's behaviour for different detunings Δ_c , particularly within and outside regions of bistability, we can assess

how collective nonlinear effects of the Rydberg vapour influence its predictive capability.

Experimental setup. In our experiment, caesium (Cs) atoms are placed inside a $(5 \times 5 \times 5) \text{ cm}^3$ heated cube glass cell, with the temperature maintained at 47.0°C , corresponding to an atomic density of $3.61 \times 10^{11} \text{ cm}^{-3}$ [36]. As shown in Fig. 1, a probe laser with wavelength 852 nm and Rabi frequency $\Omega_p/2\pi \sim 84.92 \text{ MHz}$ drives the $|6S_{1/2}, F=4\rangle \leftrightarrow |6P_{3/2}, F=5\rangle$ transition (D2 line). The coupling laser with wavelength 510 nm and Rabi frequency Ω_c is used to excite atoms to the $|48D_{5/2}\rangle$ Rydberg state. The coupling and probe lasers are aligned counter propagating in the atomic vapour cell to partially suppress Doppler broadening, forming an electromagnetically induced transparency (EIT) configuration. In this configuration, the transmission of the probe laser through the Rydberg vapour is controlled by the coupling laser [37]. The Rabi frequency Ω_c of the coupling laser is amplitude-modulated using an acousto-optic modulator (AOM) and an arbitrary waveform generator (AWG), which operates between minimal $\Omega_{\min}/2\pi \sim 2.56 \text{ MHz}$ and peak Rabi frequency $\Omega_{\max}/2\pi \sim 3.14 \text{ MHz}$. The Cs D2 line is utilized to lock the probe laser frequency, while the coupling laser frequency is stabilized to a super-stable cavity with finesse 2×10^5 . The frequency difference between coupling (probe) light and the corresponding transition $|6P_{3/2}\rangle \leftrightarrow |48D_{5/2}\rangle$ ($|6S_{1/2}\rangle \leftrightarrow |6P_{3/2}\rangle$) is defined as the detuning Δ_c (Δ_p). To measure the EIT spectrum, the frequency of the coupling light is scanned with Δ_c swept back and forth from 0 MHz to 20 MHz, while the probe light is kept resonant with the D2 line ($\Delta_p = 0$), and the probe transmission is recorded by a photodetector.

Time series prediction. We benchmark the predictive capability of the Rydberg ensemble using two qualitatively different time series: the x -component of the

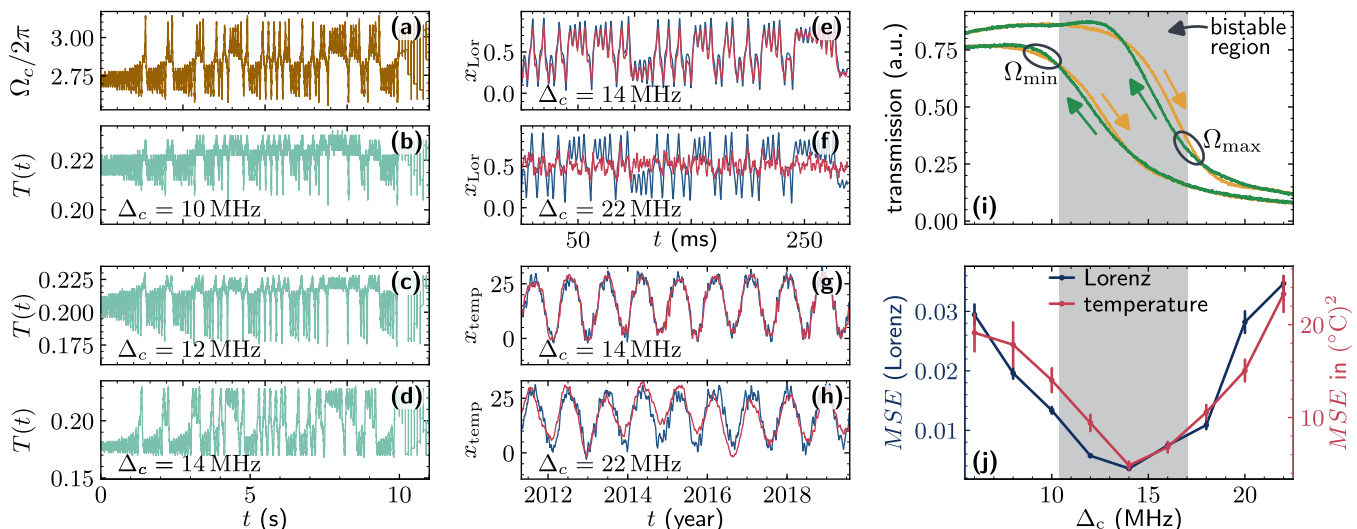


Figure 2. **Time series prediction.** (a) Amplitude modulated signal $\Omega_c/2\pi$ in MHz which is input into the Rydberg system. (b-d) Output transmission signal $T(t)$ in arbitrary units recorded for different detunings Δ_c . The detuning is chosen such that the system is out of (panel b) and within the bistable region (panels c-d). (e, f) Time series prediction for the Lorenz series x_{Lor} . A Rydberg vapour operating in the bistable region (e) results in a better prediction (red curve), compared to outside (f). The ground truth is shown in blue. (g-h) Prediction results on daily temperature of Beijing for detuning Δ_c , near (g) and out (h) of the bistable region. (i) The lower yellow and lower green curves correspond to the minimal Rabi frequency Ω_{\min} of the coupling laser but with different scan directions of the detuning Δ_c (as indicated by arrows and colours). The upper yellow and upper green curves correspond to Ω_{\max} . A closed hysteresis loop formed by the two scan directions characterizes the bistable phenomenon. The detuning interval where the bistability occurs is marked by a gray shaded box. (j) Mean square error (MSE) for varying detuning Δ_c on Lorenz and temperature time series prediction tasks. Inside the bistable region (gray shaded box), the MSE is lower than outside. The plotted MSE values correspond to the average over the 20 sampled time series, while the error bar corresponds to their standard deviation (see text for details).

the Lorenz attractor, x_{Lor} (see Methods), and the daily maximum temperature in Beijing date from 2011-01-01 to 2020-03-23, x_{temp} [38]. These examples probe the system’s performance and generalization capability across different types of data, specifically chaotic and stochastic signals.

The input signal $x(t)$ is first discretized at equidistant times t_n to obtain $x_n = x(t_n)$. Each value x_n is then mapped linearly to the interval $[\Omega_{\min}, \Omega_{\max}]$ and encoded as a time amplitude modulation in the coupling Rabi frequency $\Omega_c(t_n) \in [\Omega_{\min}, \Omega_{\max}]$, with modulation rate of 4 kHz, see Fig. 1. For the Lorenz attractor, we show a representative input signal $\Omega_c(t)$ in Fig. 2 (a). The modulated coupling laser drives the Rydberg vapour at a fixed detuning Δ_c , while the transmission $T(t)$ of the probe laser is recorded continuously. Sampling at times t_n yields a discrete output sequence $T(t_n)$ that reflects the system’s response to the input. Representative transmission traces for three characteristic detunings $\Delta_c = 10, 12,$ and 14 MHz are shown in Figs. 2(b-d), respectively: outside the bistable regime [panel (b)] and within the bistable region [panels (c,d)]. Near bistability, the signal-to-noise ratio and peak-to-peak amplitudes are visibly enhanced, indicating a stronger nonlinear response.

For the subsequent analysis, the raw transmission data $T(t_n)$ are first processed with a Savitzky–Golay filter

(window size 10, polynomial order 3 [39, 40]) to suppress high-frequency noise. To obtain several time series from a single run, we generate 20 downsampled transmission series by taking every 20th point with different initial offsets, see Fig. 1. Thus, each sub-series $T^{(i)}$ (with $i = 1, \dots, 20$) contains one out of every 20 points of the original record and has one twentieth of its length. For example, for the sub series $T^{(1)}$, the downsampled series contains 1st, 21th, 41th, ..., $(20t_n + i)$ -th points of the original record.

The prediction task is formulated using a sliding window over each downsampled series. We fix a window length $M = 200$ and, for each series i , use M consecutive transmission values as input and the next value of the downsampled time series as the prediction target. Writing

$$\vec{T}_k^{(i)} = (T_k^{(i)}, T_{k+1}^{(i)}, \dots, T_{k+M-1}^{(i)})^T \quad (1)$$

for the k -th input window, the corresponding target is chosen as

$$y_k^{(i)} = x(t_{i+20(k+M)}). \quad (2)$$

Shifting the window generates the full set of input–target pairs $(\vec{T}_k^{(i)}, y_k^{(i)})$ which are indexed by k . Thus, the input–target pairs include transmission data of the probe laser in $\vec{T}_k^{(i)}$ as well as the consecutive point of the time series

$y_k^{(i)}$ which is proportional to the Rabi frequency of the coupling laser Ω_c .

We use 70% of the input–target pairs for training and the remaining 30% for testing. For each subseries i , we train a linear regression model that maps the M -dimensional transmission window $T_k^{(i)}$ to a scalar prediction $\hat{y}_m^{(i)}$ of the next value of the original time series. Introducing a weight vector $\vec{w}^{(i)}$ and a scalar bias $b^{(i)}$, the linear regression model is defined as $\hat{y}_m^{(i)} = \vec{T}_m^{(i)} \cdot \vec{w}^{(i)} + b^{(i)}$. The parameters $\vec{w}^{(i)}$ and $b^{(i)}$ are obtained by minimizing the mean-squared error (MSE) on the training set, $\text{MSE}_{\text{train}}^{(i)} = \frac{1}{N_{\text{train}}^{(i)}} \sum_{k \in \text{train}} (y_k^{(i)} - \hat{y}_k^{(i)})^2$, where $N_{\text{train}}^{(i)}$ denotes the number of training samples in series i .

No nonlinear activation is used in this readout layer, so all nonlinear processing of the input originates from the dynamics of the Rydberg vapour itself.

Figures 2(e–h) show representative prediction results. When the system is operated within the bistable regime [Figs. 2(e), (g)], the predicted trajectories closely follow the Lorenz signal and the temperature record, including their short-time fluctuations. Outside the bistable region [Figs. 2(f), (h)], the predictions deviate substantially from the ground truth, indicating a reduced learning performance.

The dependence on detuning is summarized in Figs. 2(i,j). Figure 2(i) displays the EIT spectrum as a function of the coupling detuning Δ_c for minimal (Ω_{min}) and maximal (Ω_{max}) Rabi frequency. For each value of Ω_c , we scan Δ_c once from low to high frequency (yellow curves) and once in the opposite direction (green), and record the probe transmission as output. The upper pair corresponds to Ω_{max} , and the lower pair to Ω_{min} . Since the modulation range of Ω_c is $\Omega_c \in [\Omega_{\text{min}}, \Omega_{\text{max}}]$, a transmission region exists during the modulation of the Rabi frequency Ω_c ; for each detuning Δ_c , this region is bounded by the upper pair and lower pairs. These two branches of the transmission curve form a closed hysteresis loop: in the central gray-shaded interval, the measured transmission at a given Δ_c depends on the scan history, which signals the presence of two coexisting stable states of the Rydberg vapour. Consequently, the detuning Δ_c serves as a control parameter that characterizes the proximity of the system to the bistable region and adjusts the strength of the nonlinearity.

This bistable region is located precisely in the parameter window in which the nonlinear response of the medium is strongest and where the prediction performance of the system is found to be optimal. This is quantified by the mean squared error (MSE), averaged over the downsampled transmission series

$$\text{MSE} = \text{avg}_i \left(\frac{1}{N_{\text{pred}}^{(i)}} \sum_{k \in \text{pred}} (y_k^{(i)} - \hat{y}_k^{(i)})^2 \right). \quad (3)$$

Figure 2(j) presents the MSE as a function of detuning: the error exhibits a clear minimum inside the bistable window and increases again outside it. The error bars

denote the standard deviation over the twenty downsampled sub-series.

In summary, the Rydberg vapour shows its best prediction performance on both tasks when operated near the bistable regime adjusted by detuning Δ_c , where collective nonlinearities are most pronounced. The correlation between the EIT hysteresis and the minimum MSE points to emergent cooperative effects, rather than single-atom physics, as the key resource for enhanced learning capacity.

III. THEORETICAL MODEL

The experimental results we have just presented, reveal a correlation between improved learning capability and the regime in which the Rydberg vapour displays bistability. In order to gain understanding on this relation, we are going to describe the Rydberg vapour using a mean-field model, see e.g. Refs. [27, 31, 35], and analyse the learning capability of the modelled system.

The dilute vapour of laser-driven Rydberg atoms is modelled as N identical two-level systems with ground $|g\rangle$ and Rydberg $|e\rangle$ states (see Methods). The atoms are driven with Rabi frequency Ω and detuning Δ , while dissipation enters through spontaneous emission with rate γ and dephasing with rate γ_d . The interaction between the atoms in the Rydberg state is modelled as an all-to-all energy shift term in the Hamiltonian, i.e. $H_{\text{int}} = \frac{V}{N-1} \sum_{j < k} |e\rangle\langle e|_j |e\rangle\langle e|_k$. In the thermodynamic limit, the dynamics is described by the mean-field equations of motion for the average population $n(t) = \frac{1}{N} \sum_{j=1}^N \langle |e\rangle\langle e|_j \rangle$ and optical coherence $q(t) = \frac{1}{N} \sum_{j=1}^N \langle |e\rangle\langle g|_j \rangle$. Since in a dilute vapour at room temperature γ_d typically exceeds γ and Ω , the coherence relaxes on a much shorter timescale ($\dot{q} \gg \dot{n}$), justifying its adiabatic elimination (see Methods). Therefore, the dynamics is well described by an equation for the average Rydberg population alone. This reads

$$\dot{n} = -\frac{\Omega^2 \Gamma (n - \frac{1}{2})}{\Gamma^2 + (\Delta - nV)^2} - \gamma n =: F(n), \quad (4)$$

where we have defined the combined dissipation rate $\Gamma = \frac{1}{2}(\gamma + \gamma_d)$. This nonlinear differential equation captures the interplay of coherent driving, interactions, dephasing, and spontaneous emission. Depending on the parameter values, the model displays one or two stable solutions for the steady-state Rydberg density n_{ss} , which are shown in Fig. 3 (a).

In the experiment, the input signal is encoded by modulating the Rabi frequency. The system operates in a regime characterized by the EIT spectrum curves shown in Fig. 2(i), in which a more pronounced hysteresis is observed for larger Rabi frequencies. We find that the mean-field model displays a similar response in the stationary Rydberg density n_{ss} when operating at Rabi frequencies around the lower critical point at which the

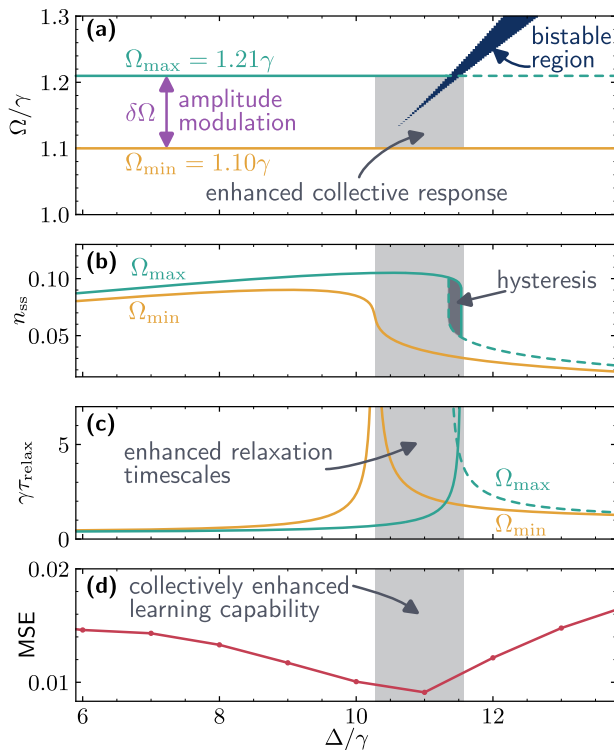


Figure 3. Mean-field dynamical response and learning capacity. (a) Phase diagram of the mean-field equation (4). The blue region marks the bistable domain where two stable stationary solutions exist. The yellow (green) horizontal lines indicate the minimum (maximum) Rabi frequency of the input signal of the learning protocol, see panel (d). The gray shadowed area indicates the region in which collective effects are most prominent for the considered Rabi frequencies. Its left (right) boundary corresponds to the detuning at which the relaxation time for the minimum (maximum) Rabi frequency displays a maximum, see panel (c). (b) Stationary Rydberg density n_{ss} for varying detuning along the horizontal cuts $\Omega/\gamma = 1.1$ and $\Omega/\gamma = 1.21$. For the case $\Omega/\gamma = 1.21$ hysteresis is observed. We denote the solution with the lower density with a dashed line. (c) Relaxation time τ_{relax} along the same cuts as in (b) for the stable stationary solutions. Within the bistable region, two relaxation times are possible, one for each stable solution. The solid (dashed) line corresponds to the solution with higher (lower) density. The longest relaxation times occur near the boundary of the bistable region. (d) Mean square error (MSE) for the prediction of the Lorenz input signal fixing the parameters to $\Omega/\gamma = 1.1$, modulation amplitude $\delta\Omega/\Omega = 0.1$, modulation period $\gamma T = 20$, noise strength $D/\gamma = 0.0001$ and for different detunings (points). In all panels $V/\gamma = 100$ and $\gamma_a/\gamma = 10$.

bistable region emerges. This is illustrated in Fig. 3(b), in which we show the stationary Rydberg densities along the maximum and minimum Rabi frequencies used in the learning protocol. In this region, collective effects result in a strong nonlinear response near the boundaries of the bistable regime, as well as hysteresis. In the presence of thermal fluctuations and noise, the strong nonlinearity

leads to an increased signal-to-noise ratio (SNR) of the system within the shadowed gray region of Fig. 3(b). In the experiment, this increased SNR is reflected by the increased peak-to-peak value from Fig. 2(b) to Fig. 2(d).

In order to theoretically analyse the correlation between these collective effects and the enhanced learning capability, we need to complement the mean-field equation (4) with a stochastic term that models the presence of noise in the experiment. We then consider the following stochastic equation for the Rydberg density: $\dot{n} = F(n) + \sqrt{nD}\xi(t)$, where $\xi(t)$ is a white noise term, and D a constant controlling its overall strength. The input signals to be predicted are then introduced analogously as in the experiment, by modulating the Rabi frequency in a piecewise fashion, with maximum modulation amplitude $\delta\Omega := \Omega_{max} - \Omega_{min} = 0.1\Omega$ and modulation period $\gamma T = 20$, see Fig. 1. The corresponding MSE for the Lorenz input is shown in Fig. 3(d) for different Δ/γ along a cut at $\Omega/\gamma = 1.1$. The MSE displays a dip around $\Delta/\gamma \sim 11$, coinciding with the region in which collective effects are most prominent, see the corresponding shadowed region in Fig. 3(b) and (d), hence supporting our previous hypothesis based on the experimental results, see Fig. 2(i) and (j). Therefore, our theoretical findings align with the experimental finding that the learning capability is improved in the bistable region, where collective effects are more prominent.

Experiment and theory also align in the observation that relaxation dynamics slows down in the regime in which the learning capability is improved. Theoretically, characteristic relaxation times, τ_{relax} , can be obtained by linearizing Eq. (4) around each of its stationary solutions, n_{ss} (see Methods). The typical behaviour of the relaxation time within the regime of operation is shown in Fig. 3(c). We observe that near the boundaries of the bistable regime, the so-called spinodal lines [27], the relaxation times increase considerably, in agreement with experimental observations (see Methods). This prolonged relaxation time is characteristic of complex systems undergoing critical behaviour and is also referred to critical slowing down [31, 41–45].

IV. CONCLUSION & OUTLOOK

In this work, we have experimentally analysed the use of a driven-dissipative Rydberg vapour at room temperature for time series prediction. By considering two different time series, we have found that the system displays an improved learning capability in the region where collective effects are stronger. These collective effects, namely strong nonlinearity and critical slowing down, originate from an underlying phase transition to a bistable regime that can be accessed by varying the Rabi frequency and detuning of the coupling laser. By modelling the experimental system with a mean-field model, we have been able to reproduce qualitatively these results, supporting the hypothesis that improved learning capability emerges

in the presence of strong collective effects.

Although an improved learning capability is observed in the bistable region, the overall achieved prediction performance in the studied Rydberg vapour is not yet competitive with established reservoir computing techniques, where significantly smaller mean square errors are reported [13, 22–24]. However, the next step could focus on the implementation of techniques from the Reservoir Computing toolbox, as time-multiplexing and feedback [46–48], in order to analyse whether these allow to improve prediction capability significantly in the Rydberg vapour setup. Future research could also investigate the relation between prolonged relaxation time and learning capacity, and the specific mechanistic role of relaxation time in mediating the learning process.

V. ACKNOWLEDGMENTS

We acknowledge the National Key R&D Program of China (Grant no. 2022YFA1404003), the Na-

tional Natural Science Foundation of China (Grants T2495252, 12104279, 123B2062, 12574318), Innovation Program for Quantum Science and Technology (Grant No. 2021ZD0302100), the Fund for Shanxi ‘1331 Project’ Key Subjects Construction, Bairen Project of Shanxi Province, supported by 111 project (Grant No. D18001), PCSIRT (No. IRT_17R70). AC acknowledges support from the Deutsche Forschungsgemeinschaft (DFG, German Research Foundation) through the Walter Benjamin programme, Grant No. 519847240. Further support was received from the DFG through the Research Units FOR 5413/1, Grant No. 465199066, and FOR 5522/1, Grant No. 499180199. We also acknowledge funding through JST-DFG 2024: Japanese-German Joint Call for Proposals on “Quantum Technologies” (Japan-JST-DFG-ASPIRE 2024) under DFG Grant No. 554561799. This work is also supported by the ERC grant OPEN-2QS (Grant No. 101164443).

-
- [1] D. Krotov, A new frontier for hopfield networks, *Nat Rev Phys* **5**, 366 (2023).
- [2] J. Kennedy and R. Eberhart, Particle swarm optimization, *ICNN’95* **4**, 1942 (1995).
- [3] K. Parsopoulos and M. Vrahatis, Recent approaches to global optimization problems through particle swarm optimization, *Nat Comput* **1**, 235 (2002).
- [4] D. Wang, D. Tan, and L. Liu, Particle swarm optimization algorithm: an overview, *Soft comput* **22**, 387 (2018).
- [5] M. Dorigo, M. Birattari, and T. Stutzle, Ant colony optimization, *IEEE Comput Intell Mag* **1**, 28 (2006).
- [6] M. Dorigo and C. Blum, Ant colony optimization theory: A survey, *Theor Comput Sci* **344**, 243 (2005).
- [7] É. Ghys, The Lorenz Attractor, a Paradigm for Chaos, in *Chaos: Poincaré Seminar 2010*, edited by B. Duplantier, S. Nonnenmacher, and V. Rivasseau (Springer, Basel, 2013) pp. 1–54.
- [8] B.-W. Shen, A Review of Lorenz’s Models from 1960 to 2008, *Int J Bifurcat Chaos* **33**, 2330024 (2023).
- [9] Y. D. Mammedov, E. U. Oluju, and G. A. Farah, Weather forecasting based on data-driven and physics-informed reservoir computing models, *Environ Sci Pollut Res Int* **29**, 24131 (2022).
- [10] H. Jaeger, Short term memory in echo state networks, Fraunhofer-Gesellschaft [10.24406/publica-fhg-291107](https://doi.org/10.24406/publica-fhg-291107) (2001).
- [11] G. Tanaka, T. Yamane, J. B. Héroux, R. Nakane, N. Kanazawa, S. Takeda, H. Numata, D. Nakano, and A. Hirose, Recent advances in physical reservoir computing: A review, *Neural Networks* **115**, 100 (2019).
- [12] K. Nakajima, Physical reservoir computing—an introductory perspective, *Jpn J Appl Phys* **59**, 060501 (2020).
- [13] C. Wringe, M. Trefzer, and S. Stepney, Reservoir computing benchmarks: A tutorial review and critique, *Int J Parallel Emergent Distrib Syst* **40**, 313 (2025).
- [14] M. Dale, J. F. Miller, S. Stepney, and M. A. Trefzer, A substrate-independent framework to characterize reservoir computers, *P Roy Soc A-math Phy* **475**, 20180723 (2019).
- [15] T. L. Carroll, Optimizing memory in reservoir computers, *Chaos* **32**, 023123 (2022).
- [16] D. J. Gauthier, E. Boltt, A. Griffith, and W. A. Barbosa, Next generation reservoir computing, *Nat commun* **12**, 5564 (2021).
- [17] M. C. Ozturk, D. Xu, and J. C. Príncipe, Analysis and design of echo state networks, *Neural Comput* **19**, 111 (2007).
- [18] C. Sun, M. Song, D. Cai, B. Zhang, S. Hong, and H. Li, A systematic review of echo state networks from design to application, *IEEE Trans Artif Intell* **5**, 23 (2024).
- [19] H. Jaeger and H. Haas, Harnessing nonlinearity: Predicting chaotic systems and saving energy in wireless communication, *Science* **304**, 78 (2004).
- [20] W. Maass, *Computability in Context* (Computer Science, 2011) pp. 275–296.
- [21] M. C. Soriano, S. Ortín, L. Keuninckx, L. Appeltant, J. Danckaert, L. Pesquera, and G. van der Sande, Delay-based reservoir computing: Noise effects in a combined analog and digital implementation, *IEEE Trans Neural Netw* **26**, 388 (2015).
- [22] K. Fujii and K. Nakajima, Harnessing Disordered-Ensemble Quantum Dynamics for Machine Learning, *Phys Rev Appl* **8**, 024030 (2017).
- [23] P. Mujal, R. Martínez-Peña, J. Norkkala, J. García-Beni, G. L. Giorgi, M. C. Soriano, and R. Zambrini, Opportunities in quantum reservoir computing and extreme learning machines, *Adv Quantum Technol* **4**, 2100027 (2021).
- [24] A. Sannia, R. Martínez-Peña, M. C. Soriano, G. L. Giorgi, and R. Zambrini, Dissipation as a resource for Quantum Reservoir Computing, *Quantum* **8**, 1291 (2024).

- [25] M. Yan, C. Huang, P. Bienstman, P. Tino, W. Lin, and J. Sun, Emerging opportunities and challenges for the future of reservoir computing, *Nat Commun* **15**, 2056 (2024).
- [26] C. Ates, T. Pohl, T. Pattard, and J. Rost, Strong interaction effects on the atom counting statistics of ultracold Rydberg gases, *J Phys B-at Mol Opt* **39**, L233 (2006).
- [27] M. Marcuzzi, E. Levi, S. Diehl, J. P. Garrahan, and I. Lesanovsky, Universal nonequilibrium properties of dissipative Rydberg gases, *Phys Rev Lett* **113**, 210401 (2014).
- [28] I. Lesanovsky and J. P. Garrahan, Out-of-equilibrium structures in strongly interacting Rydberg gases with dissipation, *Phys Rev A* **90**, 011603 (2014).
- [29] Z. Bai, C. S. Adams, G. Huang, and W. Li, Self-induced transparency in warm and strongly interacting Rydberg gases, *Phys Rev Lett* **125**, 263605 (2020).
- [30] K. Klocke, T. Wintermantel, G. Lochead, S. Whitlock, and M. Buchhold, Hydrodynamic stabilization of self-organized criticality in a driven Rydberg gas, *Phys Rev Lett* **126**, 123401 (2021).
- [31] C. Carr, R. Ritter, C. Wade, C. S. Adams, and K. J. Weatherill, Nonequilibrium phase transition in a dilute Rydberg ensemble, *Phys Rev Lett* **111**, 113901 (2013).
- [32] D.-S. Ding, H. Busche, B.-S. Shi, G.-C. Guo, and C. S. Adams, Phase diagram and self-organizing dynamics in a thermal ensemble of strongly interacting Rydberg atoms, *Phys Rev X* **10**, 021023 (2020).
- [33] K. Wadenpfuhl and C. S. Adams, Emergence of synchronization in a driven-dissipative hot Rydberg vapor, *Phys Rev Lett* **131**, 143002 (2023).
- [34] X. Wu, Z. Wang, F. Yang, R. Gao, C. Liang, M. K. Tey, X. Li, T. Pohl, and L. You, Dissipative time crystal in a strongly interacting Rydberg gas, *Nat Phys* **20**, 1389 (2024).
- [35] Z.-K. Liu, K.-H. Sun, A. Cabot, F. Carollo, J. Zhang, Z.-Y. Zhang, L.-H. Zhang, B. Liu, T.-Y. Han, Q. Li, Y. Ma, H.-C. Chen, I. Lesanovsky, D.-S. Ding, and B.-S. Shi, Emergence of subharmonics in a microwave driven dissipative Rydberg gas, *Phys Rev Res* **6**, L032069 (2024).
- [36] N. Šibalić, J. D. Pritchard, C. S. Adams, and K. J. Weatherill, Arc: An open-source library for calculating properties of alkali Rydberg atoms, *Comput Phys Commun* **220**, 319 (2017).
- [37] M. Fleischhauer, A. Imamoglu, and J. P. Marangos, Electromagnetically induced transparency: Optics in coherent media, *Rev. Mod. Phys.* **77**, 633 (2005).
- [38] Repository containing all corresponding data and source code of this manuscript, [10.5281/zenodo.XXXXXXX](https://doi.org/10.5281/zenodo.XXXXXXX) (2025).
- [39] J. Chen, P. Jönsson, M. Tamura, Z. Gu, B. Matsushita, and L. Eklundh, A simple method for reconstructing a high-quality ndvi time-series data set based on the savitzky-golay filter, *Remote Sens Environ* **91**, 332 (2004).
- [40] R. Cao, Y. Chen, M. Shen, J. Chen, J. Zhou, C. Wang, and W. Yang, A simple method to improve the quality of ndvi time-series data by integrating spatiotemporal information with the savitzky-golay filter, *Remote Sens Environ* **217**, 244 (2018).
- [41] V. Dakos, M. Scheffer, E. H. van Nes, V. Brovkin, V. Petoukhov, and H. Held, Slowing down as an early warning signal for abrupt climate change, *Proc Natl Acad Sci U S A* **105**, 14308 (2008).
- [42] M. Scheffer, J. Bascompte, W. A. Brock, V. Brovkin, S. R. Carpenter, V. Dakos, H. Held, E. H. van Nes, M. Rietkerk, and G. Sugihara, Early-warning signals for critical transitions, *Nature* **461**, 53 (2009).
- [43] P. Brookes, G. Tancredi, A. D. Patterson, J. Rahamim, M. Esposito, T. K. Mavrogordatos, P. J. Leek, E. Ginossar, and M. H. Szymanska, Critical slowing down in circuit quantum electrodynamics, *Sci Adv.* **7**, eabe9492 (2021).
- [44] J. Zhang, L.-H. Zhang, B. Liu, Z.-Y. Zhang, S.-Y. Shao, Q. Li, H.-C. Chen, Z.-K. Liu, Y. Ma, T.-Y. Han, Q.-F. Wang, C. S. Adams, B.-S. Shi, and D.-S. Ding, Early warning signals of the tipping point in strongly interacting Rydberg atoms, *Phys Rev Lett* **133**, 243601 (2024).
- [45] Y. Wang, T. Gao, Y. Niu, Y. Hu, L. Zhang, S. Jia, M. Jing, and Y. Xiao, Time delay of mean-field interaction in thermal Rydberg atomic gases, *Opt Express* **33**, 20829 (2025).
- [46] L. Appeltant, M. Soriano, G. Van der Sande, J. Danckaert, S. Massar, J. Dambre, B. Schrauwen, C. Mirasso, and I. Fischer, Information processing using a single dynamical node as complex system, *Nat Commun* **2**, 468 (2011).
- [47] H. Zhang, X. Feng, B. Li, Y. Wang, K. Cui, F. Liu, W. Dou, and Y. Huang, Integrated photonic reservoir computing based on hierarchical time-multiplexing structure, *Opt Express* **22**, 31356 (2014).
- [48] C. Sugano, K. Kanno, and A. Uchida, Reservoir computing using multiple lasers with feedback on a photonic integrated circuit, *IEEE J Sel Top Quantum Electron* **26**, 1 (2020).
- [49] E. D. Black, An introduction to Pound-Drever-Hall laser frequency stabilization, *Am J Phys* **69**, 79 (2001).
- [50] S. Juan, J. Mingxing, and J. Fei, Pound-Drever-Hall laser frequency locking technique based on orthogonal demodulation, *Optik* **168**, 348 (2018).
- [51] R. W. P. Drever, J. L. HALL, F. V. Kowalski, J. Hough, G. M. Ford, A. J. MUNLEY, and H. Ward, Laser phase and frequency stabilization using an optical resonator, *Appl Phys B-Lasers O* **31**, 97 (1983).

AUTHOR CONTRIBUTIONS STATEMENT

Z.L. conceived the idea for the study. Z.L. and Q.R. conducted the physical experiments. Z.L. and W.X. designed the learning model protocols. C.N. and A.C. simulated the theoretical model. Z.L., Q.R., C.N., A.C., W.X., Y.T., H.W., W.Y., J.X., M.J., H.Z., L.X., S.J., L.Z., and I.L. analysed the data. The manuscript was written by Z.L., Q.R., C.N., A.C., H.W., and I.L. The research were supervised by L.Z. and I.L. All authors contributed to discussions regarding the results and analysis contained in the manuscript.

VI. METHODS

Time series generation. The Lorenz oscillator $x(t)$ that we used is defined by the differential equation

$$\begin{aligned}\dot{x}(t) &= \sigma [y(t) - x(t)], \\ \dot{y}(t) &= \rho x(t) - y(t) - x(t)z(t), \\ \dot{z}(t) &= x(t)y(t) - \beta z(t),\end{aligned}\quad (5)$$

where $\sigma = 10$, $\beta = 28$, $\rho = 8/3$, time step $t_n - t_{n-1} = 0.04$ s, total time 640 s. Thus, the Rabi frequency of the coupling laser is modulated by $x(t)$ at a rate of 4 kHz per bit.

Derivation of the mean-field model. We describe the dilute vapour of Rydberg atoms as an ensemble of N two-level systems, with ground state $|g\rangle$ and Rydberg state $|e\rangle$. The dynamics is described by a Lindblad master equation for the reduced state of the system ρ ($\hbar = 1$):

$$\partial_t \rho = -i[H, \rho] + \sum_{j=1}^N (\mathcal{D}_{L_{j,s}}[\rho] + \mathcal{D}_{L_{j,d}}[\rho]), \quad (6)$$

where we have defined the dissipator $\mathcal{D}_L[\rho] = L\rho L^\dagger - \{L^\dagger L, \rho\}/2$, which models the processes of spontaneous emission and dephasing through the jump operators $L_{j,s} = \sqrt{\gamma}|g\rangle\langle e|_j$ and $L_{j,d} = \sqrt{\gamma_d}|e\rangle\langle e|_j$, respectively. The system Hamiltonian reads

$$H = -\Delta \sum_{j=1}^N |e\rangle\langle e|_j + \frac{\Omega}{2} \sum_{j=1}^N (|e\rangle\langle g|_j + |g\rangle\langle e|_j) + H_{\text{int}}, \quad (7)$$

where we model the interaction between atoms in the Rydberg state with an all-to-all energy shift: $\frac{V}{N-1} \sum_{j<k} |e\rangle\langle e|_j |e\rangle\langle e|_k$. In the thermodynamic limit, we consider the dynamics of the average Rydberg population, $n(t) = \frac{1}{N} \sum_{j=1}^N \langle |e\rangle\langle e|_j \rangle$, and average optical coherence $q(t) = \frac{1}{N} \sum_{j=1}^N \langle |e\rangle\langle g|_j \rangle$, for which we obtain the following equations of motion using the mean-field approximation:

$$\begin{aligned}\dot{n} &= \Omega \text{Im}[q] - \gamma n, \\ \dot{q} &= -i(\Delta - nV)q - \Gamma q - i\Omega(n - \frac{1}{2}),\end{aligned}\quad (8)$$

where we have omitted the time labels, denoted the derivative with respect to time with a dot, and defined $\Gamma = (\gamma + \gamma_d)/2$. Assuming $\gamma_d \gg \gamma, \Omega$, the relaxation dynamics of the average optical coherence is much faster than that of the average Rydberg population. Then, we adiabatically eliminate the coherences by setting $\dot{q} = 0$ and replacing:

$$q = -\frac{i\Omega(n - \frac{1}{2})}{i(\Delta - nV) + \Gamma} \quad (9)$$

in the dynamics of the average Rydberg population. This yields the mean-field equation presented in the main text, which is used for the numerical analysis presented there.

Theoretical analysis of the relaxation times. Relaxation times are analysed by linearizing Eq. (4) around each of its stationary solutions, i.e., introducing $n(t) = n_{\text{ss}} + \delta n(t)$ and keeping only linear terms in $\delta n(t)$. This results in a linear equation for the fluctuation dynamics, $\delta \dot{n} = -\tau_{\text{relax}}^{-1} \delta n$, where $\tau_{\text{relax}} = (\frac{\partial F(n)}{\partial n}|_{n_{\text{ss}}})^{-1}$ defines the characteristic relaxation time.

Experimental analysis of the relaxation times. In order to obtain the relaxation time of the Rydberg system τ_{relax} , we measure the transmission of the probe laser as the Rabi frequency of the coupling laser Ω_c is amplitude modulated. The amplitude modulation corresponds to a square wave with frequency 1 kHz, duty cycle 50%, and modification depth 15%. In Fig. 4(a), the detuning is swept linearly in time from 6 MHz to 22 MHz. When the detuning crosses the bistable region, the non-linear response is enhanced, while the relaxation time increases. This is analysed in more detail in Figs. 4(b)-(c), where the detuning Δ_c is fixed outside or inside the bistable region, respectively, by an ultra-stable cavity and the Pound-Drever-Hall (PDH) method [49–51]. This allows us to obtain the relaxation time by fitting the function $A \exp\{(-t/\tau) + B\}$ to every period of the transmission signal, obtaining the values $\tau_1 = 0.139$ ms, $\tau_2 = 0.148$ ms and $\tau_3 = 0.125$ ms for the data shown in panel (c). Notice that in panel (b) the relaxation times are orders of magnitude shorter.

ADDITIONAL INFORMATION

Competing interests. The authors declare no competing interests.

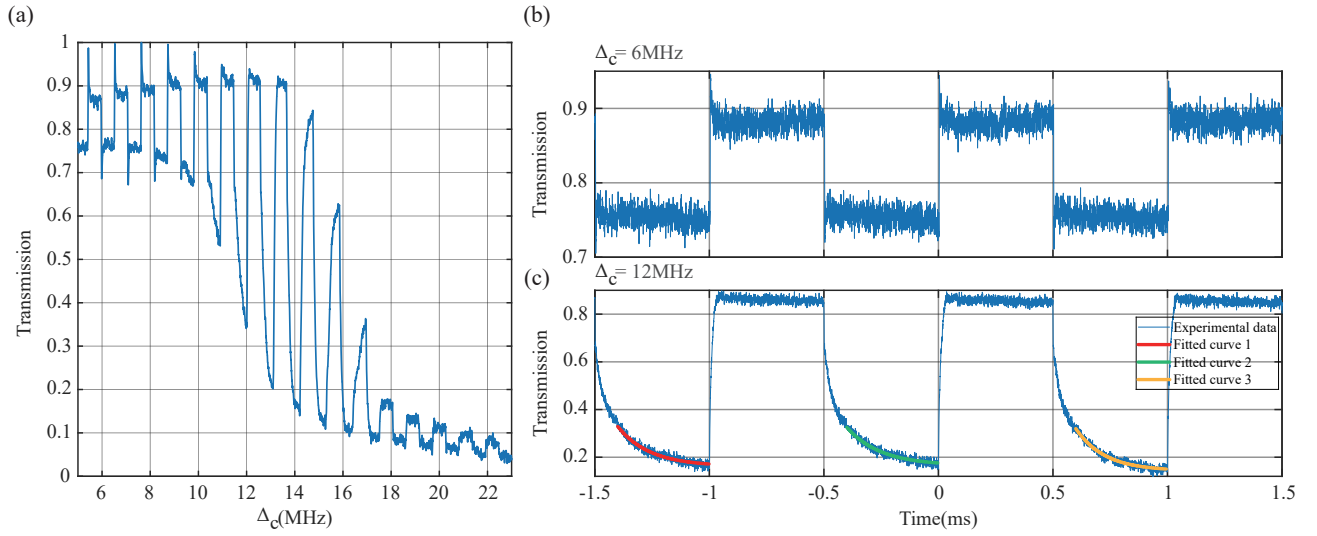


Figure 4. **Experimental analysis of the relaxation times.** Measurement of the transmission of the probe laser when the Rabi frequency Ω_c of the coupling light is amplitude modulated by a square pulse with frequency 1 kHz, duty cycle 50%, and modification depth 15%. In panel (a), the detuning of the coupling light Δ_c is swept from 6 MHz to 22 MHz linearly in time. Instead, in panels (b) and (c) the detuning is fixed to 6 MHz, and 12 MHz, respectively. Panel (b) corresponds to a point outside the bistable regime, while panel (c) to a point within the bistable regime. In panel (c) an exponential relaxation is fitted to the experimental data (see text) at three different periods obtaining the relaxation times $\tau_1 = 0.139$ ms, $\tau_2 = 0.148$ ms and $\tau_3 = 0.125$ ms.